Monthly Notices
of the
ROYAL ASTRONOMICAL SOCIETY

MNRAS **499,** 5163–5174 (2020)
Advance Access publication 2020 October 15

doi:10.1093/mnras/staa3182

# Hot gaseous atmospheres of rotating galaxies observed with *XMM–Newton*

A. Juráňová [1,2,3]★ N. Werner,[1,4,5] P. E. J. Nulsen,[6,7] M. Gaspari [8,9]† K. Lakhchaura,[10] R. E. A. Canning,[11,12] M. Donahue,[13] F. Hroch[1] and G. M. Voit[13]

[1]*Department of Theoretical Physics and Astrophysics, Masaryk University, Kotlářská 2, CZ-611 37 Brno, Czech Republic*
[2]*SRON Netherlands Institute for Space Research, Sorbonnelaan 2, NL-3584 CA Utrecht, the Netherlands*
[3]*Anton Pannekoek Institute, University of Amsterdam, Postbus 94249, NL-1090 GE Amsterdam, the Netherlands*
[4]*School of Science, Hiroshima University, 1-3-1 Kagamiyama, Higashi-Hiroshima 739-8526, Japan*
[5]*MTA-Eötvös Loránd University Lendület Hot Universe Research Group, Pázmány Péter sétány 1/A, H-1117 Budapest, Hungary*
[6]*Harvard-Smithsonian Center for Astrophysics, 60 Garden Street, Cambridge, MA 02138, USA*
[7]*ICRAR, University of Western Australia, 35 Stirling Hwy, Crawley, WA 6009, Australia*
[8]*INAF – Osservatorio di Astrofisica e Scienza dello Spazio, via P. Gobetti 93/3, I-40129 Bologna, Italy*
[9]*Department of Astrophysical Sciences, Princeton University, 4 Ivy Lane, Princeton, NJ 08544-1001, USA*
[10]*MTA-ELTE Astrophysics Research Group, Pázmány Péter sétány 1/A, H-1117 Budapest, Hungary*
[11]*Kavli Institute for Particle Astrophysics and Cosmology, Stanford University, 452 Lomita Mall, Stanford, CA 94305-4085, USA*
[12]*Department of Physics, Stanford University, 382 Via Pueblo Mall, Stanford, CA 94305-4060, USA*
[13]*Physics and Astronomy Department, Michigan State University, East Lansing, MI 48824-2320, USA*

Accepted 2020 October 9. Received 2020 October 7; in original form 2020 August 3

## ABSTRACT

X-ray emitting atmospheres of non-rotating early-type galaxies and their connection to central active galactic nuclei have been thoroughly studied over the years. However, in systems with significant angular momentum, processes of heating and cooling are likely to proceed differently. We present an analysis of the hot atmospheres of six lenticulars and a spiral galaxy to study the effects of angular momentum on the hot gas properties. We find an alignment between the hot gas and the stellar distribution, with the ellipticity of the X-ray emission generally lower than that of the optical stellar emission, consistent with theoretical predictions for rotationally supported hot atmospheres. The entropy profiles of NGC 4382 and the massive spiral galaxy NGC 1961 are significantly shallower than the entropy distribution in other galaxies, suggesting the presence of strong heating (via outflows or compressional) in the central regions of these systems. Finally, we investigate the thermal (in)stability of the hot atmospheres via criteria such as the TI- and *C*-ratio, and discuss the possibility that the discs of cold gas present in these objects have condensed out of the hot atmospheres.

**Key words:** galaxies: active – galaxies: elliptical and lenticular, cD – X-rays: galaxies.

## 1 INTRODUCTION

Many massive early-type galaxies are permeated by hot gas, but its long-lasting presence, the role of the central supermassive black hole, and the relation to colder gas phases have not been fully understood (for a recent review see Werner et al. 2019). Effects of significant net angular momentum of the X-ray atmospheres could be of considerable importance to the current view, affecting mostly relatively lower mass host galaxies (Eskridge, Fabbiano & Kim 1995; Sarzi et al. 2013; Negri, Ciotti & Pellegrini 2014a; Negri et al. 2014b; Gaspari, Brighenti & Temi 2015; DeFelippis et al. 2020).

So far, most X-ray studies have focused on the hot atmospheres permeating massive slow rotating giant elliptical galaxies. However, around 80 per cent of the 260 early-type galaxies in the ATLAS$^{3D}$ sample are regular rotators (Krajnović et al. 2011), which often have flattened discy morphologies. Interestingly, observations revealed that the X-ray luminosity, $L_X$, of an early-type galaxy is related to its morphology, determined by its distribution of stars. Derived ratios of $L_X/L_B$ (to reduce the dependence on stellar mass) for 'pure' ellipticals were found to be systematically higher than those of 'discy' ellipticals and lenticulars (Eskridge et al. 1995; Sarzi et al. 2013). The flattened shape of the gravitational potential and rotational support, which has been confirmed for flattened early-type galaxies (Emsellem et al. 2011), should allow easier development of outflows. Furthermore, it has been shown by Pellegrini (2012) that in low-mass systems, the energy injection through supernovae can become dominant and thus have a significant effect on the properties of their X-ray haloes (see also e.g. David, Forman & Jones 1990; Mathews & Brighenti 2003).

According to both observations and theoretical predictions, cool and cold gas in brightest cluster galaxies is thought to be a product of cooling from the hot intracluster medium (e.g. Johnstone, Fabian & Nulsen 1987; Heckman et al. 1989; Bridges & Irwin 1998; Conselice, Gallagher & Wyse 2001; McDonald, Veilleux & Mushotzky 2011; Gaspari, Tombesi & Cappi 2020, for a recent review) and partly a product of stellar mass-loss (Voit & Donahue 2011). About half of the nearby X-ray bright giant elliptical galaxies contain H $\alpha$ + [N II]

★ E-mail: a.juranova@sron.nl
† Lyman Spitzer Jr. Fellow

emitting gas that most likely cooled from the hot X-ray atmospheres (Lakhchaura et al. 2018). Recent surveys focusing on CO emission in early-type galaxies (Combes, Young & Bureau 2007; Young et al. 2011; Davis et al. 2019) found the presence of molecular gas in approximately 25 per cent of studied objects. For the ATLAS$^{3D}$ sample, Young et al. (2011) found no correlation of the molecular gas mass with stellar (*K*-band) luminosity, which implies that the molecular gas does not originate purely in stellar mass-loss. Babyk et al. (2019) found a correlation between the mass of the X-ray atmosphere and molecular hydrogen content. Molecular hydrogen was reported in systems with cooling times as short as $10^9$ yr (e.g. Temi et al. 2018), indicating the conditions are right for condensation of cool, dense gas from hot atmospheres.

Hydrodynamic simulations of rotationally supported systems predict that cooling from the hot phase should lead to the formation of multiphase discs (Gaspari et al. 2015). Recent *XMM–Newton* observations of the rotating lenticular galaxy, NGC 7049, support this proposition. In the otherwise isothermal gas, spectral signatures of ongoing cooling were detected in a region cospatial with the plane of rotation of the galaxy as well as a multiphase disc ranging from warm gas to a cold molecular phase (Juráňová et al. 2019).

Here, we focus on the properties of a sample of hot atmospheres permeating six rotationally supported lenticular galaxies and a massive spiral galaxy and compare our findings with non-rotating systems. The paper is structured as follows. In Section 2.3, we present the selected objects and describe the analysis of the *XMM–Newton* EPIC observations used. The main results are shown in Section 3, specifically focusing on the morphology of the hot gas (3.1) and its thermodynamic properties (3.2), and we address the thermal stability of the hot atmospheres (3.3). In Section 4, we discuss our findings and present our conclusions in Section 5.

## 2 THE SAMPLE AND DATA REDUCTION

### 2.1 The sample

To study the properties of the hot gas in rotating galaxies, we searched the volume-limited ATLAS$^{3D}$ sample (Cappellari et al. 2011) for systems where the 2D maps of line-of-sight stellar velocities indicate ordered rotation (classified as 'regular rotators' in Krajnović et al. 2011) and the *XMM–Newton* archive contains sufficient data to determine the gas density and temperature in at least three concentric annular regions. All objects selected in our sample have the ratio of rotational velocity to velocity dispersion greater than 1/3 (see Table 1). All galaxies in the ATLAS$^{3D}$ sample are located at a distance $d < 42$ Mpc, which allows us to perform a spatially resolved analysis of their extended X-ray emitting atmospheres with *XMM–Newton*. The sensitivity of *XMM–Newton* in the 0.3–2 keV band, where most of the X-rays emitted by S0 galaxies emerge, makes this satellite uniquely suited for the study of these systems.

The selection resulted in six S0 galaxies and the X-ray bright spiral galaxy NGC 1961. Optical images of the whole sample are shown in Fig. 1. The most important properties of these galaxies are listed in Tables 1 and 2. Their available *XMM–Newton* observations, denoted by observation IDs (OBSIDs), are listed in Table A1.

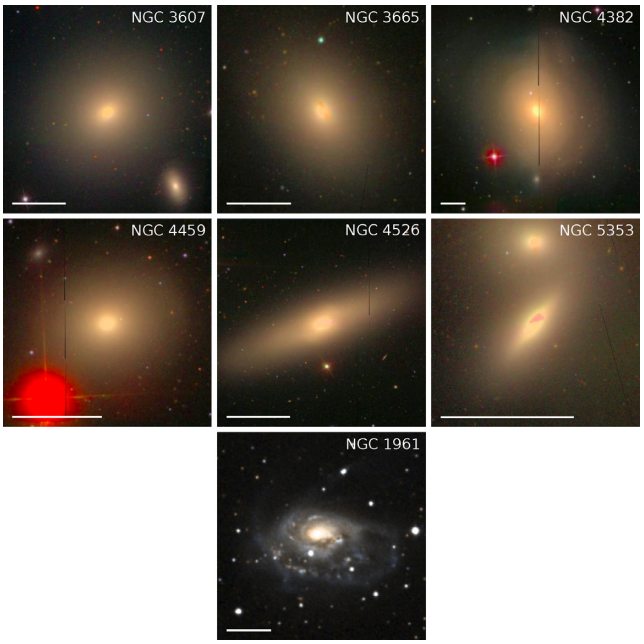


**Figure 1.** Optical images of the studied sample of S0 galaxies and NGC 1961. The images are taken from Sloan Digital Sky Survey (SDSS, data release 7) with the exception of NGC 1961, which is from Digitized Sky Survey 2. The SDSS images are compositions of *g*, *r*, and *i* (Smith et al. 2002) imaging data. The solid line in the lower left corner of every image represents a scale of 10 kpc.

**Table 1.** Basic observational properties of the studied sample. Distance *d* is adopted from the ATLAS$^{3D}$ project and references therein with the exception of NGC 1961, where the median value of distances from NED was taken, as well as values for redshift ($z$) in the second column. Where given, the values of $M_{200}$ were determined from globular clusters kinematics or the total mass of galaxy's globular clusters and published by Kim et al. (2019) except for NGC 1961, where it was determined from the maximal stellar rotation velocity by Bogdán et al. (2013). The effective radii $R_e$ and stellar velocity dispersions and rotational velocities are adopted from Cappellari et al. (2011).

| Object NGC | $d$ Mpc | $z$ $10^{-3}$ | Scale arcsec kpc$^{-1}$ | $R_e$ kpc | log $M_{200}$ $M_\odot$ | $\sigma_{v,\star}$ km s$^{-1}$ | $v_{rot,\star}$ km s$^{-1}$ |
|---|---|---|---|---|---|---|---|
| 3607 | 22.2 | 3.14 | 9.29 | 4.24 | 12.85 | 222.0 ± 4.0 | 110.0 ± 9.0 |
| 3665 | 33.1 | 6.90 | 6.23 | 3.43 | – | 215.0 ± 8.5 | 94.3 ± 21.5 |
| 4382 | 17.9 | 2.43 | 11.52 | 9.93 | 13.13 | 68.3 ± 16.5 | 176.0 ± 3.5 |
| 4459 | 16.1 | 3.98 | 12.81 | 2.82 | 12.67 | 75.0 ± 20.0 | 171.8 ± 4.8 |
| 4526 | 16.4 | 2.06 | 12.58 | 3.66 | 12.87 | 150.4 ± 8.6 | 246.0 ± 6.0 |
| 5353 | 35.2 | 7.75 | 5.86 | 2.58 | – | 298.0 ± 9.0 | 284.0 ± 4.8 |
| 1961 | 32.4 | 13.12 | 6.37 | 8.06 | 13.08 | 242.0 ± 12.0 | 326.8 ± 9.5 |

**Table 2.** Multiwavelength properties of the analysed sample. *B*-band stellar luminosities $L_B$ and *B*–*V* colour indexes are taken from HyperLEDA (Makarov et al. 2014), 1.4 GHz radio powers from Brown et al. (2011) and Condon, Cotton & Broderick (2002), PAH luminosities from Kokusho et al. (2017) and Stierwalt et al. (2014) in the case of NGC 1961, masses of molecular hydrogen from Young et al. (2011) and Combes et al. (2009) for NGC 1961, masses of atomic hydrogen from Young et al. (2014), Haynes et al. (2018) for NGC 4526 and Haan et al. (2008) for NGC 1961. Star formation rates are taken from Amblard et al. (2014) and Davis (2014).

| Object NGC | $L_B$ $10^{10}\,L_{B,\odot}$ | *B*–*V* mag | $\log P_{\rm radio}$ W Hz$^{-1}$ | $L_{\rm PAH}$ $10^{41}$ erg s$^{-1}$ | $\log M_{\rm H_2}$ $M_\odot$ | $\log M_{\rm HI}$ $M_\odot$ | SFR $M_\odot$ yr$^{-1}$ |
|---|---|---|---|---|---|---|---|
| 3607 | 3.70 | 0.93 | 20.63 | $7.8 \pm 6.2$ | 8.42 | <6.53 | 0.420 |
| 3665 | 3.37 | 0.93 | 22.04 | $45.1 \pm 9.9$ | 8.91 | <7.05 | 0.109 |
| 4382 | 5.86 | 0.89 | <19.79 | $0.3 \pm 5.5$ | <7.39 | <6.59 | 0.002 |
| 4459 | 1.45 | 0.97 | <19.63 | $7.1 \pm 2.9$ | 8.24 | <6.53 | 0.071 |
| 4526 | 2.42 | 0.98 | 20.61 | $17.1 \pm 4.4$ | 8.59 | 7.15 | 0.028 |
| 5353 | 3.56 | 1.03 | 21.62 | $2.3 \pm 6.7$ | <7.44 | <7.07 | 0.095 |
| 1961 | 22.91 | 0.86 | 22.82 | $37.8 \pm 3.1$ | 10.39 | 10.67 | 9.24 |

#### 2.1.1 NGC 3607

NGC 3607 is an unbarred lenticular galaxy (morphological type SA0) and the brightest of the 18 member galaxies of the Leo II group (Giuricin et al. 2000). It has the highest star formation rate (SFR) in our sample, 0.42 $M_\odot$yr$^{-1}$ (Amblard et al. 2014). The presence of a rotating disc of cold molecular gas in NGC 3607 was confirmed from measurements of CO emission (Alatalo et al. 2013). *Chandra X-ray Observatory* measurements do not show evidence for an X-ray bright AGN.

#### 2.1.2 NGC 3665

Another SA0 type galaxy in our sample, NGC 3665, is the brightest member of a group of 11 galaxies (Makarov & Karachentsev 2011). Of our sample, it has the highest luminosity emerging as emission features of polycyclic aromatic hydrocarbons (PAH; Kokusho et al. 2017), triggered by absorption of far-ultraviolet light indicating a relatively high SFR. However, the SFR measured by other methods (Amblard et al. 2014) in this system is still relatively low, at $\sim$ 0.1 $M_\odot$ yr$^{-1}$. A rotating cold molecular disc reaching out to $\sim$3 kpc from the centre of the galaxy was detected by Alatalo et al. (2013). NGC 3665 is among our radio brightest S0s at 1.4 GHz and is the only one in our sample that shows a pronounced radio activity associated with an AGN. Twin jets were observed by the Very Large Array (VLA) (Parma et al. 1986), as well as core radio emission at 5 GHz (Liuzzo et al. 2009). The mass of the supermassive black hole was measured by Onishi et al. (2017) to be $M_\bullet = 5.8 \times 10^8$ $M_\odot$.

#### 2.1.3 NGC 4382

This object, also known as M 85, resides in the Virgo cluster. Its distance to the cluster centre is, however, almost 6 deg, which is well outside the virial radius of Virgo. It is the only galaxy in our sample, which does not have a disc of cold gas near its centre. The morphological type of this galaxy is SA0 and the galaxy also shows shell-like structures. These features are formed by the stars of smaller infalling galaxies, due to the combined effects of Liouville's theorem and phase wrapping (Quinn 1984). The lack of cold gas is consistent with the observed low SFR of 0.002 $M_\odot$ yr$^{-1}$ (Amblard et al. 2014).

Capetti et al. (2009) found that the core of NGC 4382 does not show any radio emission related to a central black hole. The current scaling $M_\bullet$–$L$ (Kormendy 1993) predict a black hole mass of $M_\bullet = 1.7 \times 10^9$ $M_\odot$, an estimate recently published by Graham & Soria (2019), who also identified an X-ray point source ($L_{\rm X,AGN} = 8 \times 10^{38}$ erg s$^{-1}$) revealed by *Chandra* observations as a counterpart to the central black hole.

#### 2.1.4 NGC 4459

Another member of the Virgo cluster, NGC 4459, is an unbarred lenticular galaxy with a dusty disc extending out to $r \sim 0.7$ kpc, with observed blue clumps suggesting the presence of newborn stars (Ferrarese et al. 2006). Unable to detect any neutral hydrogen in their observations, Lucero & Young (2013) provide only an upper limit on its mass, $M_{\rm HI} < 1.7 \times 10^7$ $M_\odot$, despite the clear presence of molecular hydrogen (see Table 2), yielding a ratio $M_{\rm H_2}/M_{\rm HI} > 21$. Far- and mid-infrared emission of gas was studied in detail by Young, Bendo & Lucero (2009) and led to a detection of 24 μm emission from a disc reaching out to $r \sim 2.6$ kpc, which exceeds almost four times the radius of the dusty structures and thus cannot be attributed to ongoing star formation. They also find that NGC 4459 has a so-called FIR-excess, i.e. FIR-to-radio flux density ratio exceeding a value of 3.04, a rare feature defined from observations of a large sample of galaxies in Yun, Reddy & Condon (2001). In the centre of NGC 4459, Gavazzi et al. (2018) report a detection of H $\alpha$ emission. An X-ray image from *Chandra* revealed a point source identified as the central AGN ($L_{\rm X,AGN} = 10^{39}$ erg s$^{-1}$; Gallo et al. 2010).

#### 2.1.5 NGC 4526

The only barred lenticular galaxy (SAB) in our sample, NGC 4526, is also a member of the Virgo Cluster, but again outside the cluster virial radius. Having two entries in the New General Catalogue, it is also known as NGC 4560. Hereafter, we will only use the designation NGC 4526 for this object, which is also preferred in the scientific community. It is oriented nearly edge-on and also possesses a dusty disc in the plane of rotation, spanning over the central $r \sim 1.2$ kpc. The SFR in NGC 4526 is the smallest among galaxies with a dusty disc in our sample (Amblard et al. 2014) and the PAH luminosity the second highest, $\sim 17 \times 10^{41}$ erg s$^{-1}$ (Kokusho et al. 2017). As in the case of NGC 4459, Lucero & Young (2013) did not detect neutral hydrogen and only placed the upper limit of $M_{\rm HI} < 1.9 \times 10^7$ $M_\odot$, while the total mass of $H_2$ was measured well (see Table 2). The lower limit of their ratio is thus even larger than in NGC 4459: $M_{\rm H_2}/M_{\rm HI} > 100$. Focusing on the warm gas content, Gavazzi et al. (2018) found H $\alpha$ emission with a disc-like morphology in this galaxy. Davis et al.

(2013) measured the mass of the central supermassive black hole to be $M_\bullet = 4.5 \times 10^8$ $M_\odot$.

#### 2.1.6 NGC 5353

This almost edge-on galaxy is a member of the compact group, HCG 68, with NGC 5350, NGC 5354, and two more objects (Hickson 1982), accompanied by another 45 fainter galaxies and more member candidates (Tully & Trentham 2008). It has an effective radius of only $\sim 3.4$ kpc, which is smaller than any of the other five lenticular galaxies in our study. O'Sullivan et al. (2018) found a CO disc with a radius of 0.8 kpc accompanied by a dusty disc in the central $r \sim 0.5$ kpc (Goullaud et al. 2018). This object is classified as a low-ionization nuclear emission-line region (LINER) galaxy (e.g. Saikia et al. 2018). Sánchez-Sutil et al. (2006) reported an X-ray bright nuclear point source spatially coincident with a radio source, which can be associated with the central AGN.

#### 2.1.7 NGC 1961

This rotation-dominated spiral galaxy is the brightest member of a small group of seven galaxies (Tempel et al. 2016) and it has been classified as a LINER (Carrillo et al. 1999). Measurements of rotational velocity at distances exceeding 10 kpc from the galaxy centre (Rubin, Ford & Roberts 1979) have revealed that this spiral galaxy is exceptionally massive, and X-ray observations showing a point source located in the centre of the galaxy confirm the presence of an AGN (Roberts & Warwick 2000). The total mass of the galaxy is more than sufficient to retain its hot gaseous atmosphere, which has been observed by both *Chandra* and *XMM–Newton* (Anderson & Bregman 2011; Bogdán et al. 2013). Bogdán et al. (2013) compared available observations of NGC 1961 with results from numerical simulations finding that the galaxy is dark matter dominated – baryons contribute only 11 per cent of the total mass. In radio observations at 6 and 18 cm presented in Krips et al. (2007), nuclear emission is accompanied by a $\sim 2\sigma$ signal resembling radio jets. Additionally, distorted HI morphology revealed that the gas is being stripped by the surrounding intragroup medium (Shostak et al. 1982).

### 2.2 Data reduction

The data were reduced with the standard procedures of the *XMM–Newton* Science Analysis System version 17.0.0. Event lists from raw-data files were obtained using tasks `emchain` for EPIC-MOS and `epchain` for EPIC-pn. For EPIC-pn, we also created models of events received during readout (so-called out-of-time events). For this step, the `epchain` task was run for a second time to obtain the out-of-time (OOT) event list, which was, after proper scaling, subtracted from the pn events. Parts of the observations are affected by the so-called soft-proton flares. To filter out the affected time periods, we excluded the data where the count rate deviated from the mean by more than $1.5\sigma$. The total and the filtered net exposure times, $t_{\rm tot}$ and $t_{\rm net}$, respectively, are given in Table A1.

The extraction of images was performed using the ESAS package (Snowden & Kuntz 2011) in the 0.3–2.0 keV band.

To study the thermodynamic properties of the X-ray emitting gas, we extracted spectra from several concentric annuli. If the number of photons was sufficiently high, the width of the annuli was determined by the angular resolution of *XMM–Newton*. For the innermost annuli, the width was typically 15 arcsec ($\sim 1.2 \times$ the FWHM of the EPIC-pn or $\sim 3.4 \times$ the FWHM of the EPIC-MOS).

Typically, X-ray point sources of various origin are projected on to the extended emission of interest. To avoid their undesired contribution to the spectra, we encircled the emission of each point source and excluded the selected events during the spectral extraction procedure. As none of the X-ray atmospheres of interest covered the entire field of view, it was possible to create a spectrum of local background to be subtracted prior to spectral analysis.

### 2.3 Spectral analysis

The spectra are fitted in the $0.5 - 5.0$ keV range. Events in the $1.38 - 1.60$ keV range were excluded due to contamination by instrumental lines (e.g. Carter & Read 2007).

In the following sections, we present results from both projected and deprojected spectra, focusing primarily on the latter. For the analysis of projected spectra, we used the SPEX spectral fitting package (Kaastra, Mewe & Nieuwenhuijzen 1996) version 3.04.00, which uses an extensive atomic data base SPEXACT (version 2.07.00). SPEX allows fitting using the C-statistic (Cash 1979), defined for Poissonian distribution of data. This is particularly useful for spectra with a low number of counts in a large set of bins, because the use of C-statistic does not require extensive binning. The data were binned to contain at least one count per bin. The spectra were deprojected using the so-called Direct X-ray Spectral Deprojection (DSDEPROJ; Russell, Sanders & Fabian 2008). Using this method, the spectra extracted from individual annuli are properly subtracted from those lying closer to their common centre. Unfortunately, the deprojected spectra could not be fitted using C-statistic, so $\chi^2$ minimization was used instead. These spectra are binned to at least 25 counts per bin.

As the X-ray emitting gas can be described as a dilute plasma in collisional ionization equilibrium (CIE), we used the corresponding model `cie` in SPEX. At the energy resolution of EPIC, the spectral properties are set mainly by the gas temperature, emission measure, which translates to a normalization of the spectrum, and elemental abundances. As the latter were not well-constrained by the spectral fits, we assumed the Solar relative abundances of Lodders, Palme & Gail (2009) and fixed the metallicity to 0.5 $Z_\odot$. We note that a bias in the overall metallicity would affect the derived physical quantities as follows: a factor of two difference in the measured and actual metallicity would result in 25 per cent bias in the gas density, and 17 per cent in the entropy. Slopes of radial profiles would be altered by less than 10 per cent in the presence of metallicity gradients (Werner, Allen & Simionescu 2012).

The fact that the gas temperature is not constant over the investigated volume of the atmosphere was accounted for by the parameter `sig` in the `cie` model. When non-zero, this parameter changes the model from single- to multitemperature with a Gaussian distribution and the root-mean-square width equal to `sig`. Even though the assumption of a Gaussian temperature distribution does not necessarily reflect the true temperature distribution accurately, it still serves as a good approximation and adds only one free parameter to our model. The parameter `sig` was left free during fitting when a single-temperature model did not provide a good fit.

The unresolved population of low-mass X-ray binaries (LMXBs) was modelled with a power-law component with spectral index 1.6, in accordance with Irwin, Athey & Bregman (2003). Most of the atmospheric X-ray emission of galaxies is observed below 2.0 keV, while the more energetic photons provide a constraint on the LMXB contribution.

The X-ray emission from both the hot gas and the LMXBs is absorbed by Galactic gas with solar abundances. For each object, we fix the Galactic absorption column density to the value determined by

**Table 3.** Total hydrogen column densities taken from Kalberla et al. (2005).

| Object | $N_{\rm H}$ ($10^{20}$ cm$^{-2}$) |
|---|---|
| NGC 1961 | 11.7 |
| NGC 3607 | 1.36 |
| NGC 3665 | 2.00 |
| NGC 4382 | 2.54 |
| NGC 4459 | 2.67 |
| NGC 4526 | 1.47 |
| NGC 5353 | 0.954 |

the Leiden/Argentine/Bonn (LAB) Survey of Galactic H I (Table 3; Kalberla et al. 2005).

In the following sections, the results are given with $1\sigma$ error bars.

## 3 RESULTS

### 3.1 Imaging analysis

To study the overall morphology of the galactic atmospheres, we created images in the $0.3-2.0$ keV band. The background subtracted, exposure corrected and adaptively smoothed images are shown in Fig. 2. The signal is displayed on a logarithmic scale so that the hot atmospheres are visible out to their outskirts. Bright point sources are removed in the same manner as for the spectral analysis

To determine the flattening of the atmospheres, we used the CIAO (version 4.12; Fruscione et al. 2006) fitting tool SHERPA (Refsdal et al. 2009) to fit each galaxy with a 2D $\beta$-model (Cavaliere & Fusco-Femiano 1976, 1978) of the form

$$I(r) = I_{\rm c}\left[1+r^2\right]^{-3\beta/2}, \tag{1}$$

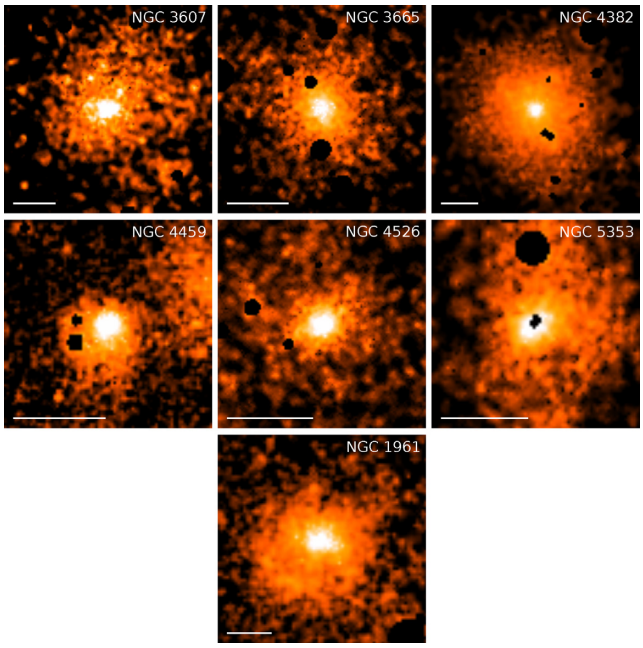


**Figure 2.** Images of X-ray atmospheres of S0 galaxies in our sample and NGC 1961, all extracted in the energy range $0.3-2.0$ keV. The images are displayed on log-scale in order to visualize the full extent of the hot atmospheres, while the most prominent point sources have been removed. The solid line in the lower-left corner of every image represents a scale of 10 kpc.

where

$$r^2 = \frac{(1-\varepsilon_{\rm X})^2\tilde{x}^2+\tilde{y}^2}{r_0^2(1-\varepsilon_{\rm X})^2} \tag{2}$$

and

$$\tilde{x} = (x-x_{\rm c})\cos\theta + (y-y_{\rm c})\sin\theta,$$
$$\tilde{y} = (y-y_{\rm c})\cos\theta - (x-x_{\rm c})\sin\theta. \tag{3}$$

The normalization $I_{\rm c}$, the $\beta$ parameter, the centre of the emission [$x_{\rm c}$, $y_{\rm c}$], position angle $\theta$, core radius $r_0$, and ellipticity $\varepsilon_{\rm X}$ were all left free. The X-ray emission was fitted out to the last annulus presented in this work. Best-fitting values of the $\beta$ parameter, $r_0$, $\varepsilon_{\rm X}$ and position angle $\mathrm{PA_X} = \theta + 90^\circ$ are listed in Table 4 along with the ellipticity and position angle of the stellar component taken from the literature. It is immediately obvious that the position angles of the X-ray gas and stellar distributions are generally similar. The measured ellipticity is on average lower for the X-ray gas (the mean ratio of the X-ray gas and stellar ellipticity is $\overline{\varepsilon_{\rm X}/\varepsilon_\star} = 0.6\pm0.3$) and does not correlate directly with the ellipticity of the stellar component.

The X-ray morphologies of NGC 3607 and NGC 4459 show the presence of a tail indicating ram-pressure stripping by the ambient intracluster/group medium or an interaction with a nearby galaxy. An X-ray source seen to the right of NGC 4459 in Fig. 2 (unrelated emission of a distant galaxy cluster) has been excluded from the analysis. Regarding past AGN activity, no prominent features are visible in the diffuse emission, nor can be identified in available *Chandra* observations.

### 3.2 Thermodynamic properties

#### 3.2.1 *Gas mass and temperature*

First, we fitted the X-ray emission within 2–6 $R_{\rm e}$ for all galaxies with a single- or multitemperature model, depending on the spectrum (see Section 2.3), to obtain the global properties of the hot gas. The radial extent of the analysed emission was set by the data quality and the maximal radius corresponds to the outer edge of the last annulus presented in this work (see Table 5). Best-fitting parameters derived from this fit are listed in Table 5, where the Gaussian width of the temperature distribution of the multitemperature model is denoted as $\sigma_{\rm T_X}$ and is presented for spectra where this model provides an improved fit.

We estimated the total gas mass $M_{\rm X}$ of the hot atmosphere by summing the gas masses calculated for each shell from the particle number densities $n$ derived from the deprojected spectra.

The summation has been performed out to the last annulus presented in this work and the resulting masses are given in Table 5. For the density profiles, see Fig. A1 in the Appendix.

The best-fitting radial temperature distributions obtained from both projected and deprojected spectra are presented in Fig. 3. The spiral galaxy is plotted in a lighter shade of blue to be easily distinguishable from lenticulars. Monotonically radially decreasing temperature profiles are present in NGC 4382 and NGC 1961, while clearly outwardly increasing temperature is only observed in NGC 3607. The profiles of NGC 3665, 4459, and 4526 do not show any significant trends and within $3\sigma$ uncertainties are close to being isothermal.

To test whether the results are affected by the instrumental PSF, we performed an equivalent analysis using *Chandra* data of NGC 4526 (following the analysis procedures of Lakhchaura et al. 2018), the object with the steepest X-ray brightness profile in our sample. The

**Table 4.** X-ray ellipticity ($\varepsilon_X$), position angle ($PA_X$), parameter $\beta$, and core radius ($r_0$) determined from $\beta$-model fitting and their optical counterparts, $\varepsilon_\star$ and $PA_\star$, from Krajnović et al. (2011) and Jarrett et al. (2003) in the case of NGC 1961, for which the uncertainty has not been published.

| NGC | $\varepsilon_X$ | $\varepsilon_\star$ | $PA_X$ (deg) | $PA_\star$ (deg) | $\beta$ | $r_0$ (pc) |
|---|---|---|---|---|---|---|
| 3607 | $0.144 \pm 0.011$ | $0.13 \pm 0.08$ | $119.7 \pm 2.3$ | $124.8 \pm 7.6$ | $0.440 \pm 0.007$ | $35 \pm 2$ |
| 3665 | $0.175 \pm 0.005$ | $0.22 \pm 0.01$ | $29.0 \pm 1.0$ | $30.9 \pm 2.0$ | $0.643 \pm 0.008$ | $142 \pm 3$ |
| 4382 | $0.110 \pm 0.006$ | $0.25 \pm 0.07$ | $29.8 \pm 1.7$ | $12.3 \pm 11.0$ | $0.349 \pm 0.004$ | $31 \pm 2$ |
| 4459 | $0.060 \pm 0.016$ | $0.21 \pm 0.03$ | $134.1 \pm 7.8$ | $105.3 \pm 1.9$ | $0.79 \pm 0.06$ | $58 \pm 4$ |
| 4526 | $0.218 \pm 0.005$ | $0.76 \pm 0.05$ | $116.8 \pm 0.7$ | $113.7 \pm 1.2$ | $1.00 \pm 0.02$ | $129 \pm 3$ |
| 5353 | $0.253 \pm 0.004$ | $0.48 \pm 0.04$ | $136.6 \pm 0.6$ | $140.4 \pm 4.9$ | $0.86 \pm 0.01$ | $157 \pm 3$ |
| 1961 | $0.161 \pm 0.009$ | 0.330 | $100.8 \pm 1.8$ | $92.0 \pm 2.0$ | $0.46 \pm 0.01$ | $63 \pm 3$ |

**Table 5.** Total X-ray gas luminosities, emission-weighted temperatures, and gas masses. Where a single temperature model did not provide a good fit, a multitemperature model with a Gaussian emission measure distribution was used and the best-fitting value of the parameter $\sigma_{T_X}$ is presented. In the last column, the radius within which the spectra were extracted is given.

| Object NGC | $L_X$ $10^{40}$ erg s$^{-1}$ | $k_BT_X$ keV | $\sigma_{T_X}$ keV | $M_X$ $10^9$ M$_\odot$ | $R_{max}$ kpc |
|---|---|---|---|---|---|
| 3607 | 1.74 | $0.411^{+0.025}_{-0.009}$ | – | $1.52^{+0.07}_{-0.17}$ | 21.8 |
| 3665 | 2.30 | $0.312^{+0.006}_{-0.006}$ | – | $1.09^{+0.07}_{-0.07}$ | 19.1 |
| 4382 | 7.97 | $0.316^{+0.025}_{-0.024}$ | $0.012^{+0.017}_{-0.012}$ | $5.26^{+0.10}_{-0.10}$ | 36.1 |
| 4459 | 0.31 | $0.390^{+0.041}_{-0.014}$ | – | $0.12^{+0.02}_{-0.02}$ | 9.3 |
| 4526 | 0.71 | $0.260^{+0.013}_{-0.019}$ | – | $0.15^{+0.03}_{-0.02}$ | 8.5 |
| 5353 | 4.21 | $0.651^{+0.020}_{-0.020}$ | $0.225^{+0.042}_{-0.046}$ | $0.49^{+0.03}_{-0.03}$ | 11.7 |
| 1961 | 4.79 | $0.298^{+0.030}_{-0.082}$ | $0.202^{+0.082}_{-0.053}$ | $6.01^{+0.49}_{-0.46}$ | 25.8 |

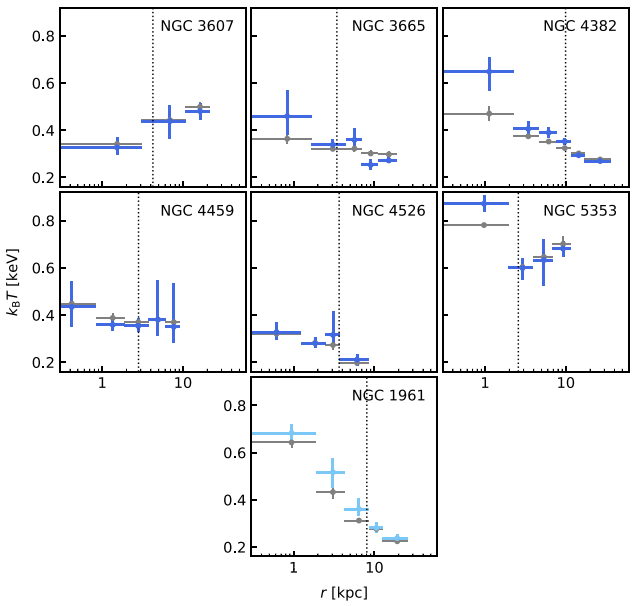


**Figure 3.** Radial, azimuthally averaged temperature profiles derived from projected (grey) and deprojected (blue) spectra with metallicity fixed at 0.5 Z$_\odot$. For clarity, dark blue points represent S0 galaxies in our sample, while the profile of the spiral galaxy NGC 1961 is plotted in light blue. The effective radius (see Table 1) is represented by the black dotted line in each panel.

widths of the analysed annuli are at least 30 times larger than the angular resolution of *Chandra*. The obtained results agree with those presented in this work and therefore we expect the *XMM–Newton* PSF to have a negligible effect on our findings.

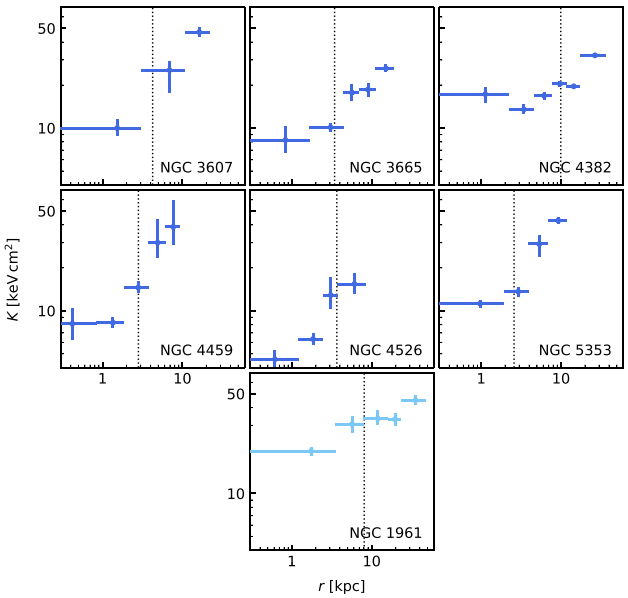


**Figure 4.** Entropy profiles (see equation 4) derived from deprojected spectra.

### 3.2.2 *Entropy*

A key physical quantity describing the thermodynamic states of hot galactic atmospheres is entropy. We adopt here its definition customary in this field and refer to the entropy index $K$ defined below as the entropy hereafter,

$$K \equiv k_B T n_e^{-2/3}. \quad (4)$$

This definition relates to the thermodynamic entropy per particle, $s$, of non-interacting monoatomic particles as $\Delta s = 3/2 k_B \ln K$. A gravitationally stratified atmosphere in hydrostatic equilibrium should have an entropy profile rising monotonically with radius, while a flat or decreasing trend would indicate a convectively unstable environment.

The entropy distribution for all analysed galaxies is plotted in Fig. 4, separately. For a clearer comparison with elliptical galaxies, the entropy profiles of S0s are plotted in Fig. 5 together with the results obtained for a sample of 49 giant ellipticals presented by Lakhchaura et al. (2018). In general, the central entropy of the lenticulars lies above the values observed in most of the slow-rotating elliptical galaxies.

Purely gravitational heating would result in an entropy profile given by $K \propto r^{1.1}$, which is usually not observed due to the heating by the AGN and supernovae that centrally increase the gas entropy, flattening the profiles to $K \propto r^{0.67}$ (Panagoulia, Fabian & Sanders

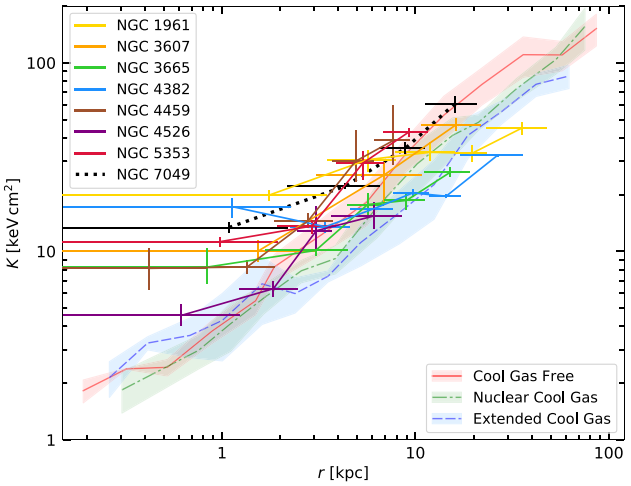


**Figure 5.** Entropy profiles of the rotationally supported galaxies in this study (solid lines), NGC 7049, an S0 from previous work (black dotted line Juráňová et al. 2019) and a sample of elliptical galaxies distinguished by the extent of cool gas of Lakhchaura et al. (2018). For the ellipticals, lines signify median profiles and surrounding shaded regions the median absolute deviations.

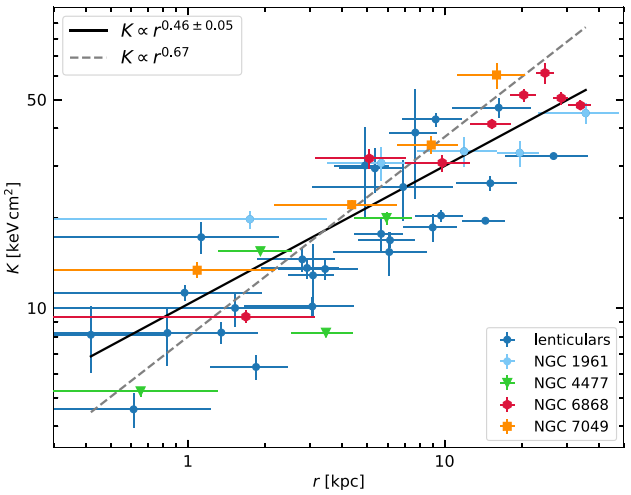


**Figure 6.** Entropy profiles of rotationally supported galaxies in this study together with profiles of NGC 4477 (Li et al. 2018), NGC 7049 (Juráňová et al. 2019), and NGC 6868 (Werner et al. 2014; Lakhchaura et al. 2018). The black line represents a best-fitting power-law model determined from a fit of all plotted data points. The grey dashed line illustrates the profile usually observed in X-ray atmospheres (see the text for more detailed discussion).

2014; Babyk et al. 2018). To quantify the amount of flattening in rotating atmospheres, we fitted the average entropy profiles of all S0 galaxies in our sample with a power-law model, together with the fast-rotating spiral NGC 1961 and also including the galaxies NGC 4477 (Li, Su & Jones 2018), NGC 7049 (Juráňová et al. 2019), and NGC 6868 (Werner et al. 2014; Lakhchaura et al. 2018), which show discs of warm/cold gas indicative of rotational support. The resulting average power-law index $\Gamma = 0.46 \pm 0.05$ and the corresponding best-fitting curve is plotted together with the data in Fig. 6. The scatter is, however, large and the flattest entropy profiles are observed in NGC 1961 and NGC 4382, with slopes of $\Gamma = 0.24 \pm 0.05$ and $\Gamma = 0.3 \pm 0.1$, respectively. After excluding these two galaxies and the last two data points of NGC 6868 the average

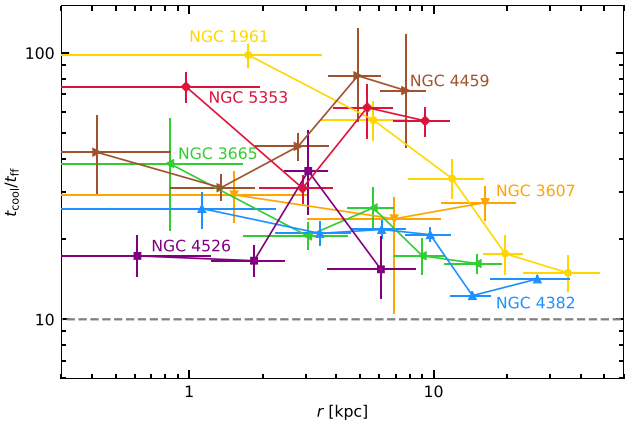


**Figure 7.** Ratio of cooling time to free-fall time for all studied galaxies. The value $t_{cool}/t_{ff} \approx 10$ (see Section 3.3) is visualized as a dashed grey line.

entropy profile becomes $\Gamma = 0.64 \pm 0.06$, consistent with Babyk et al. (2018).

### 3.3 Thermal stability

Higher central entropy suggests recent heating and gas expulsion. AGN activity has been confirmed in NGC 3665 and *Chandra* observations show an X-ray point source in the centre of NGC 3607, NGC 3665, NGC 4459, and NGC 4526. Therefore, to address the thermal stability of the gas, we computed cooling time profiles, which are shown in Fig. A2 in the Appendix. We computed $t_{cool}$ as

$$t_{cool} = \frac{3}{2} \frac{(n_e + n_i) k_B T}{n_e n_i \Lambda(T, Z)}, \quad (5)$$

where the electron and ion densities are denoted as $n_e$ and $n_i$, respectively, and $\Lambda(T)$ stands for the cooling function. In addition to cooling time alone, profiles of cooling time to free-fall time ratio were derived from the observed thermodynamic properties. The free-fall time was computed under the assumption of hydrostatic equilibrium, using gravitational acceleration

$$g = -\frac{1}{\rho}\frac{dp}{dr} = -\frac{1}{n m_H \mu}\frac{dp}{dr}, \quad (6)$$

where $\mu$ is the mean atomic weight, $\mu = 0.62$, and $m_H$ is the mass of a hydrogen atom. The particle number density was calculated as $n = 1.92\, n_e$, where the electron number density, $n_e$, was obtained directly from the spectrum normalization. The values of the pressure ($p = nk_BT$) gradient were determined from a fit by a $\beta$-profile or a power law, when required by the shape of the pressure profile. The resulting values are presented in Fig. 7 for all eight studied objects and separately in the Appendix, Fig. A3. The value of $t_{cool}/t_{ff} = 10$ is visualized through a dashed grey line and is exceeded at all radii. Despite the confirmed presence of cold gas, the values of $t_{cool}/t_{ff}$ at small radii correspond to values observed in cool gas free galaxies (e.g. Voit et al. 2015; Hogan et al. 2017).

We also inspected the thermal stability of the hot gas using a parameter that compares the cooling time with a time-scale related to turbulent motions in the gas. It has been proposed that when these two time-scales become comparable, the physical conditions in the hot atmosphere should favour development of multiphase gas. We compute this quantity, the so-called *C*-ratio, as $C \equiv t_{cool}/t_{eddy}$ (see

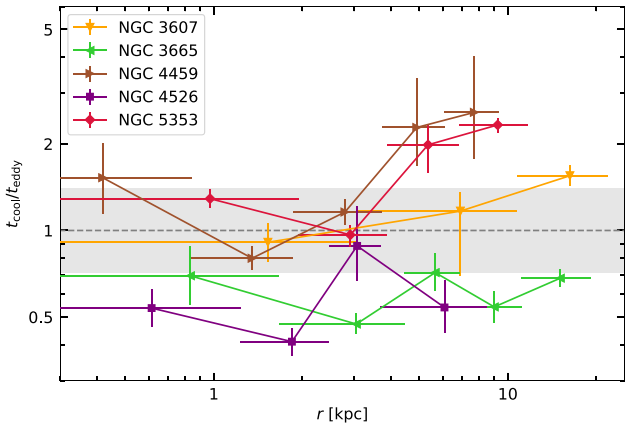


**Figure 8.** The $C$-ratio (see Section 3.3) of S0 galaxies possessing cold gas. The grey region represents the $1\sigma$ confidence region (from hydrodynamical simulations; Gaspari et al. 2018) where conditions for the development of multiphase condensations are expected to be favourable.

Section 5.2. in Gaspari et al. 2018), where

$$t_{\rm eddy} = 2\pi \frac{r^{2/3} L^{1/3}}{\sigma_{v,L}} \quad (7)$$

and where $\sigma_{v,L}$ is the gas velocity dispersion at injection scale $L$ (typically 5–10 kpc). According to Gaspari et al. (2018), this distance can be estimated as a diameter of the cold/warm phase, and the corresponding $\sigma_{v,L}$ can be obtained by extrapolating the measured $\sigma_v$ of the cold gas. For the galaxies in our sample, the velocity dispersions in the cold gas have not been published. Nevertheless, to have at least an estimate of this condensation parameter, we adopt the value of the velocity dispersion measured in NGC 7049, $\sigma_{v,L} = 36\,{\rm km\,s^{-1}}$ (Juráňová et al. 2019). The results computed for S0 galaxies with discs of cold gas are plotted in Fig. 8 and show that the conditions in these hot atmospheres are favourable for condensation from the hot phase. We note that the multiphase condensation is expected to occur along helical orbits settling on to a disc where the gas rotational speed exceeds the gas velocity dispersion, i.e. turbulent Taylor number ${\rm Ta_t} > 1$ (Gaspari et al. 2015). Conversely, and typically within the inner kpc region (see NGC 7049; Juráňová et al. 2019), we expect ${\rm Ta_t} < 1$ and thus a more chaotic cold accretion rain. Forthcoming high-resolution optical and radio observations of warm and cold gas (e.g. via MUSE and ALMA) will be key to unveil the detailed top-down multiphase condensation kinematics.

## 4 DISCUSSION

### 4.1 Hot gas morphology and mass

The projected flattening of the hot atmospheres has been found to be similar to or smaller than that of the stellar component in all studied objects (see Table 4), in agreement with the hydrodynamical simulations of e.g. Brighenti et al. (2009), Negri et al. (2014b), and Gaspari et al. (2015). The ellipticity has been measured using background and point source subtracted X-ray images, which are, however, contaminated by the X-ray emission of unresolved stellar sources, potentially contributing to the observed flattening. However, given that the X-ray emission in the $0.3 - 2.0$ keV band is dominated by the gaseous atmosphere, the ellipticity is primarily due to the distribution of the diffuse gas. The principal axes of the ellipsoidal isophotes fitted to the X-ray and optical emission are aligned within the measured uncertainties. This result is consistent with ordered rotation of the X-ray atmosphere in a generally rounder total gravitational potential. We note that, however, a similar effect would also be expected for non-rotating gas in a gravitational potential that is flattened due to rotation. Assuming a spherically symmetric gravitational potential, we attempted to place an upper limit on the rotational velocity, but, unfortunately, we found that the quality of the data analysed is insufficient to place any useful constraint on it. The assumption of spherical symmetry in the subsequent analysis is not expected to affect our results significantly. The ellipticity of the X-ray atmospheres is low and the logarithmic scale in Fig. 2 strongly emphasizes features deviating from the azimuthal symmetry of the atmospheres.

The amount of observed hot gas in S0 galaxies, which has been derived from deprojected densities out to 2–6 $R_{\rm e}$, varies from $10^8$ to $5 \times 10^9$ M$_\odot$. Several authors (e.g. Brighenti et al. 2009; Negri et al. 2014b; Gaspari et al. 2015) have shown that the hot atmospheres of rotationally supported galaxies have smaller hot gas content, lower emission-weighted temperatures, and thus lower X-ray luminosities. The largest amount of atmospheric gas has been found in NGC 1961 and NGC 4382, and is comparable to the hot gas content in slow-rotating giant ellipticals (Werner et al. 2012; Babyk et al. 2019).

### 4.2 Thermodynamic properties

#### *4.2.1 Temperature*

Radial azimuthally averaged profiles reveal that the hot gas temperature is systemically lower in the S0 galaxies than in giant ellipticals (see e.g. Lakhchaura et al. 2018). This is an expected outcome, as the virial temperature of less massive S0 galaxies is lower and the ordered stellar motion in rotating systems leads to less effective heating of the gas ejected in stellar mass-loss. The radially decreasing temperature profile of NGC 1961 suggests central heating, which can be provided by adiabatic heating, the AGN, or by supernovae, exploding relatively frequently due to the star formation of $\sim 10\,{\rm M_\odot\,yr^{-1}}$.

A negative temperature gradient is observable also in NGC 4382. The energy input via type Ia SNe can be estimated from their expected rate, which for a galaxy of this stellar mass ($M_\star = 4 \times 10^{11}$ M$_\odot$; Gallo et al. 2010) and SFR (see Table 2) corresponds to approximately $0.02\,{\rm yr^{-1}}$ using a relation from Sullivan et al. (2006), or $0.01\,{\rm yr^{-1}}$, when derived from the $B$-band luminosity (Pellegrini 2012). Assuming a kinetic energy of $E_{\rm SNIa} \approx 10^{51}$ erg per supernova, this rate corresponds to a time-averaged energy injection of $6 \times 10^{41}\,{\rm erg\,s^{-1}}$ or $3 \times 10^{41}\,{\rm erg\,s^{-1}}$, respectively. Such heating would be sufficient to compensate for the energy losses of the hot gas if the efficiency of SN heating was at least $\sim 12$ per cent or $\sim 27$ per cent, respectively. An additional contribution of the merger event that led to the creation of shells is expected to be of lesser importance. According to cosmological numerical simulations analysed by Pop et al. (2018), the initial interaction of the progenitors occurred $4 - 8$ Gyr ago and most of the stars were stripped $\sim 2$ Gyr ago, while the central cooling time measured in NGC 4382 is $t_{\rm cool} \approx 0.5$ Gyr.

#### *4.2.2 Entropy*

The central entropy in most of the studied S0 galaxies is above that of elliptical galaxies, indicating the presence of a centrally positioned heating mechanism. The low star formation rate suggests that energy injection via winds of young stars and core-collapse supernovae is

most likely incapable of providing the required energy. A plausible source of energy could be the central AGN or type Ia supernovae.

The average radial entropy distribution of the rotating galaxies in our sample shown in Fig. 6 appears to be shallower than the entropy profiles in galaxy clusters and slow-rotating giant ellipticals. The power-law index of the average radial profile is $\Gamma = 0.46 \pm 0.05$. The scatter in the profiles is, however, large and the dominant heating mechanism might differ from galaxy to galaxy. The flattest entropy profiles are observed in NGC 4382 ($\Gamma = 0.3 \pm 0.1$) and the massive spiral galaxy NGC 1961 ($\Gamma = 0.24 \pm 0.05$). The entropy profiles for the rest of the sample have an index $\Gamma = 0.64 \pm 0.06$, consistent with the results of Babyk et al. (2018). However, the central entropy for all systems in our sample appears higher than the typical values measured in slow rotating giant ellipticals (Lakhchaura et al. 2018).

The relatively flat entropy profiles are consistent with the presence of outflows in the rotationally supported atmospheres. As the outflows redistribute the gas from the central region towards the outskirts, reducing the central gas-mass fraction, the entropy profiles will become shallower. This can be achieved more easily if rotation lowers the effective binding energy (albeit anisotropically) and thus facilitates matter ejection from the core regions.

### 4.3 Thermal stability

The central cooling times do not exceed $\sim 0.5$ Gyr and remain as low as $\sim 1$ Gyr out to 10 kpc in all investigated galaxies, confirming that feedback is necessary to stabilize these hot atmospheres. The observed cooling times at 10 kpc are consistent with the findings of Babyk et al. (2019). These results, along with direct traces of AGN activity in several objects in our sample, raise the question of thermal stability of the hot gas.

The calculations of the *C*-ratio (Gaspari et al. 2018) shown in Fig. 8 suggest that turbulence could, in principle, be capable of generating density fluctuations prone to cooling. This conclusion depends on our assumption of the velocity dispersion, as the $t_{\rm eddy}$ scales with $\sigma_{v,L}^{-1}$. Velocity dispersions have been estimated from resonant scattering and line broadening by Ogorzalek et al. (2017) in several elliptical galaxies using spectra from the *XMM–Newton* Reflection Grating Spectrometer. The average best-fitting 3D $\sigma_v$ is approximately 190 km s$^{-1}$ (however, none of the galaxies studied by Ogorzalek et al. 2017, is a fast rotator).

Rotational support has a radical effect on the thermal stability of the hot gas. In a spherical system, with no rotation, the negative buoyancy of a cool gas clump causes it to fall inward towards the place where it is neutrally buoyant. At that location, the mean heating rate matches the cooling rate, so it is in thermal balance. Even if the heating from a central AGN is anisotropic, the tendency for the gas to find the place where it is neutrally buoyant will cause gas that is overheated to move outwards and be replaced by inflowing gas that has previously been underheated, bringing that gas closer to the AGN, where the heating is greater, potentially driving large scale circulation. As a result, it is relatively difficult for thermal instability to grow, whenever $t_{\rm cool}$ significantly exceeds $t_{\rm ff}$ (i.e. TI-ratio $\gg$1).

This may change when there is appreciable rotational support. A gas clump will generally not have the same density as the ambient gas at the place where it is dynamically stable, so that it no longer naturally finds the place where the ambient heating rate matches its cooling rate. Since the gas distribution is no longer spherical, a spherically symmetric heating rate cannot maintain thermal balance. Rotating gas will tend to cool into a disc, rather than being fed into the AGN. In the absence of significant stellar feedback, this means that there is far more opportunity for the gas to cool into a disc. Indeed, a more relevant condensation criterion in this rotating scenario is the *C*-ratio. As shown in Fig. 8, this is found to hover around *C*-ratio $\sim$1, which is the condensation zone for direct turbulent condensation (Gaspari et al. 2018). This can occur independently of very high TI-ratios (up to 100, as found here), with the formation of a multiphase disc or a chaotic cold accretion rain set by $\rm Ta_t > 1$ or $<1$, respectively.

Interestingly, the two galaxies with the greatest gas mass (NGC 1961 and NGC 4382) have the shallowest entropy profiles and the greatest entropy levels in their centres. Assuming that the atmospheres of these galaxies are close to hydrostatic equilibrium, their nearly isentropic profiles will be responsible for the observed pronounced central temperature peaks.

The shallow entropy profiles are most likely the result of strong central feedback activity. For stellar feedback, where heating is dominated by core collapse supernovae, to operate, stars would need to have formed within the past cooling time. However, as shown in Table 2, there is no evidence for significant recent star-formation in the investigated galaxies. Once the feedback raises the central entropy level, the heat input from SNIa can exceed the radiative cooling rate within a radius of several kpc (Voit et al. 2015, 2020) and the energy input of SN Ia from older stars (the SN Ia activity is not part of any feedback loop) might even help to drive galactic winds.

The cold gas reservoir could, in principle, also be replenished by stellar ejecta. According to e.g. Voit & Donahue (2011), the gas ejected from stars should heat up and mix with the hot phase in systems with as low central density and star formation rate as in our investigated S0 galaxies. However, the presence of cold gas with PAH molecules suggests a non-negligible role of winds of asymptotic giant branch stars in the cold gas production. A plausible explanation has been recently presented by Li, Bryan & Quataert (2019) based on 3D hydrodynamical simulations. They suggest that cooling from the hot phase could be induced in the mixing layer of the dusty stellar wind and the surrounding hot gas, leading to the preservation of these fragile particles.

## 5 CONCLUSIONS

We presented a study of the X-ray emitting atmospheres of six lenticulars and one massive spiral galaxy to study the effects of angular momentum on the properties of the hot gas. We compare the measured thermodynamic properties with a sample of ellipticals in which the rotational support is negligible.

We find an alignment between the hot gas and the stellar distribution, with the ellipticity of the X-ray emission generally lower than that of the optical stellar emission, consistent with theoretical predictions for rotationally supported hot atmospheres. Two galaxies in the investigated sample, NGC 4382 and the massive spiral NGC 1961 have remarkably flat entropy profiles with $\Gamma \approx 0.2$–0.3, suggesting the presence of outflows in the central regions of these systems. These two galaxies also have significantly higher atmospheric gas masses than the other systems in our sample and their gas content is similar to that observed in slow rotating giant ellipticals (e.g. Werner et al. 2012; Babyk et al. 2019). The entropy profiles for the rest of the sample have an index $\Gamma = 0.64 \pm 0.06$, consistent with the results of Babyk et al. (2018). However, the central entropy for all systems in our sample appears higher than the typical values measured in slow rotating giant ellipticals (Lakhchaura et al. 2018).

Investigating the relation between hot atmospheres and the observed cold gas phases, we present the derived dimensionless

parameters broadly adopted as being related to the thermal stability of hot atmospheres. We obtain a ratio of cooling time to free-fall time of $t_{\rm cool}/t_{\rm ff} \gtrsim 10$ for all objects. We also estimate the ratio of the cooling and turbulent time-scales and discuss the possibility that the discs of cold gas present in these objects have condensed out from the hot atmospheres, preliminarily finding *C*-ratios around unity which are favourable for non-linear turbulent condensation (e.g. Gaspari et al. 2018).

## ACKNOWLEDGEMENTS

AJ is partially supported by the Netherlands Organisation for Scientific Research (NWO) through the Aspasia grant connected to the Innovational Research Incentives Scheme Vidi grant 016.143.312. The Space Research Organisation of the Netherlands is financially supported by NWO. NW was supported by the Lendület LP2016-11 grant awarded by the Hungarian Academy of Sciences and is currently supported by the MUNI Award for Science and Humanities funded by the Grant Agency of Masaryk University. MG acknowledges partial support by the Lyman Spitzer Jr. Fellowship (Princeton University) and by National Aeronautics Space Administration (NASA) Chandra GO8-19104X/GO9-20114X and *HST* GO-15890.020-A grants. Based on observations obtained with *XMM–Newton*, an European Space Agency (ESA) science mission with instruments and contributions directly funded by ESA Member States and NASA. This research has made use of the NASA/IPAC Extragalactic Database (NED), which is operated by the Jet Propulsion Laboratory, California Institute of Technology, under contract with NASA, and software provided by the Chandra X-ray Center in the application packages CIAO and SHERPA.

## DATA AVAILABILITY

The data underlying this article will be shared on reasonable request to the corresponding author.

## REFERENCES

Alatalo K. et al., 2013, MNRAS, 432, 1796
Amblard A., Riguccini L., Temi P., Im S., Fanelli M., Serra P., 2014, ApJ, 783, 135
Anderson M. E., Bregman J. N., 2011, ApJ, 737, 22
Babyk I. V., McNamara B. R., Nulsen P. E. J., Russell H. R., Vantyghem A. N., Hogan M. T., Pulido F. A., 2018, ApJ, 862, 39
Babyk I. V., McNamara B. R., Tamhane P. D., Nulsen P. E. J., Russell H. R., Edge A. C., 2019, ApJ, 887, 149
Bogdán Á. et al., 2013, ApJ, 772, 97
Bridges T. J., Irwin J. A., 1998, MNRAS, 300, 967
Brighenti F., Mathews W. G., Humphrey P. J., Buote D. A., 2009, ApJ, 705, 1672
Brown M. J. I., Jannuzi B. T., Floyd D. J. E., Mould J. R., 2011, ApJ, 731, L41
Capetti A., Kharb P., Axon D. J., Merritt D., Baldi R. D., 2009, AJ, 138, 1990
Cappellari M. et al., 2011, MNRAS, 413, 813
Carrillo R., Masegosa J., Dultzin-Hacyan D., Ordoñez R., 1999, Rev. Mex. Astron. Astrofis., 35, 187
Carter J. A., Read A. M., 2007, A&A, 464, 1155
Cash W., 1979, ApJ, 228, 939
Cavaliere A., Fusco-Femiano R., 1976, A&A, 49, 137
Cavaliere A., Fusco-Femiano R., 1978, A&A, 70, 677
Combes F., Young L. M., Bureau M., 2007, MNRAS, 377, 1795
Combes F. et al., 2009, A&A, 503, 73
Condon J. J., Cotton W. D., Broderick J. J., 2002, AJ, 124, 675
Conselice C. J., Gallagher J. S. I., Wyse R. F. G., 2001, AJ, 122, 2281
David L. P., Forman W., Jones C., 1990, ApJ, 359, 29
Davis T. A., 2014, MNRAS, 445, 2378
Davis T. A., Bureau M., Cappellari M., Sarzi M., Blitz L., 2013, Nature, 494, 328
Davis T. A., Greene J. E., Ma C.-P., Blakeslee J. P., Dawson J. M., Pandya V., Veale M., Zabel N., 2019, MNRAS, 486, 1404
DeFelippis D., Genel S., Bryan G. L., Nelson D., Pillepich A., Hernquist L., 2020, ApJ, 895, 17
Emsellem E. et al., 2011, MNRAS, 414, 888
Eskridge P. B., Fabbiano G., Kim D.-W., 1995, A&AS, 97, 141
Ferrarese L. et al., 2006, A&AS, 164, 334
Fruscione A. et al., 2006, in Silva D. R., Doxsey R. E., eds, Proc. SPIE Conf. Ser. Vol. 6270, Observatory Operations: Strategies, Processes, and Systems. SPIE, Bellingham, p. 62701V
Gallo E., Treu T., Marshall P. J., Woo J.-H., Leipski C., Antonucci R., 2010, ApJ, 714, 25
Gaspari M., Brighenti F., Temi P., 2015, A&A, 579, A62
Gaspari M. et al., 2018, ApJ, 854, 167
Gaspari M., Tombesi F., Cappi M., 2020, Nat. Astron., 4, 10
Gavazzi G., Consolandi G., Pedraglio S., Fossati M., Fumagalli M., Boselli A., 2018, A&A, 611, A28
Giuricin G., Marinoni C., Ceriani L., Pisani A., 2000, ApJ, 543, 178
Goullaud C. F., Jensen J. B., Blakeslee J. P., Ma C.-P., Greene J. E., Thomas J., 2018, ApJ, 856, 11
Graham A. W., Soria R., 2019, MNRAS, 484, 794
Haan S., Schinnerer E., Mundell C. G., García-Burillo S., Combes F., 2008, AJ, 135, 232
Haynes M. P. et al., 2018, ApJ, 861, 49
Heckman T. M., Baum S. A., van Breugel W. J. M., McCarthy P., 1989, ApJ, 338, 48
Hickson P., 1982, ApJ, 255, 382
Hogan M. T., McNamara B. R., Pulido F., Nulsen P. E. J., Russell H. R., Vantyghem A. N., Edge A. C., Main R. A., 2017, ApJ, 837, 51
Irwin J. A., Athey A. E., Bregman J. N., 2003, ApJ, 587, 356
Jarrett T. H., Chester T., Cutri R., Schneider S. E., Huchra J. P., 2003, AJ, 125, 525
Johnstone R. M., Fabian A. C., Nulsen P. E. J., 1987, MNRAS, 224, 75
Juráňová A. et al., 2019, MNRAS, 484, 2886
Kaastra J. S., Mewe R., Nieuwenhuijzen H., 1996, in Yamashita K., Watanabe T., eds, UV and X-ray Spectroscopy of Astrophysical and Laboratory Plasmas. Universal Academy Press, Tokyo, p. 411
Kalberla P. M. W., Burton W. B., Hartmann D., Arnal E. M., Bajaja E., Morras R., Pöppel W. G. L., 2005, A&A, 440, 775
Kim D.-W., James N., Fabbiano G., Forbes D., Alabi A., 2019, MNRAS, 488, 1072
Kokusho T., Kaneda H., Bureau M., Suzuki T., Murata K., Kondo A., Yamagishi M., 2017, A&A, 605, A74
Kormendy J., 1993, in Beckman J., Colina L., Netzer H., eds, IAU Symposium, Vol. 153, Galactic Bulges, Springer, Dordrecht, p. 209
Krajnović D. et al., 2011, MNRAS, 414, 2923
Krips M. et al., 2007, A&A, 464, 553
Lakhchaura K. et al., 2018, MNRAS, 481, 4472
Li Y., Su Y., Jones C., 2018, MNRAS, 480, 4279
Li Y., Bryan G. L., Quataert E., 2019, ApJ, 887, 41
Liuzzo E., Giovannini G., Giroletti M., Taylor G. B., 2009, A&A, 505, 509
Lodders K., Palme H., Gail H.-P., 2009, Landolt-Börnstein, Vol. 4B, Springer-Verlag, Berlin, p. 560
Lucero D. M., Young L. M., 2013, AJ, 145, 56
Makarov D., Karachentsev I., 2011, MNRAS, 412, 2498
Makarov D., Prugniel P., Terekhova N., Courtois H., Vauglin I., 2014, A&A, 570, A13
Mathews W. G., Brighenti F., 2003, ARA&A, 41, 191
McDonald M., Veilleux S., Mushotzky R., 2011, ApJ, 731, 33
Negri A., Ciotti L., Pellegrini S., 2014a, MNRAS, 439, 823
Negri A., Posacki S., Pellegrini S., Ciotti L., 2014b, MNRAS, 445, 1351
O'Sullivan E. et al., 2018, A&A, 618, A126
Ogorzalek A. et al., 2017, MNRAS, 472, 1659

Onishi K., Iguchi S., Davis T. A., Bureau M., Cappellari M., Sarzi M., Blitz L., 2017, MNRAS, 468, 4663
Panagoulia E. K., Fabian A. C., Sanders J. S., 2014, MNRAS, 438, 2341
Parma P., de Ruiter H. R., Fanti C., Fanti R., 1986, A&AS, 64, 135
Pellegrini S., 2012, in Kim D.-W., Pellegrini S., eds, Hot Interstellar Matter in Elliptical Galaxies, ASSL, Vol. 378, Springer-Verlag, New York, p. 21
Pop A.-R., Pillepich A., Amorisco N. C., Hernquist L., 2018, MNRAS, 480, 1715
Quinn P. J., 1984, ApJ, 279, 596
Refsdal B. L. et al., 2009, in Varoquaux G., van der Walt S., Millman J., eds, Proceedings of the 8th Python in Science Conference. Pasadena, CA USA, p. 51
Roberts T. P., Warwick R. S., 2000, MNRAS, 315, 98
Rubin V. C., Ford W. K. J., Roberts M. S., 1979, ApJ, 230, 35
Russell H. R., Sanders J. S., Fabian A. C., 2008, MNRAS, 390, 1207
Saikia P., Körding E., Coppejans D. L., Falcke H., Williams D., Baldi R. D., Mchardy I., Beswick R., 2018, A&A, 616, A152
Sánchez-Sutil J. R., Muñoz-Arjonilla A. J., Martí J., Garrido J. L., Pérez-Ramírez D., Luque-Escamilla P., 2006, A&A, 452, 739
Sarzi M. et al., 2013, MNRAS, 432, 1845
Shostak G. S., Hummel E., Shaver P. A., van der Hulst J. M., van der Kruit P. C., 1982, A&A, 115, 293
Smith J. A. et al., 2002, AJ, 123, 2121
Snowden S. L., Kuntz K. D., 2011, American Astronomical Society Meeting Abstracts #217, 344.17
Stierwalt S. et al., 2014, ApJ, 790, 124
Sullivan M. et al., 2006, ApJ, 648, 868
Temi P., Amblard A., Gitti M., Brighenti F., Gaspari M., Mathews W. G., David L., 2018, ApJ, 858, 17
Tempel E., Kipper R., Tamm A., Gramann M., Einasto M., Sepp T., Tuvikene T., 2016, A&A, 588, A14
Tully R. B., Trentham N., 2008, AJ, 135, 1488
Voit G. M., Donahue M., 2011, ApJ, 738, L24
Voit G. M., Donahue M., O'Shea B. W., Bryan G. L., Sun M., Werner N., 2015, ApJ, 803, L21
Voit G. M. et al., 2020, ApJ, 899, 70
Werner N., Allen S. W., Simionescu A., 2012, MNRAS, 425, 2731
Werner N. et al., 2014, MNRAS, 439, 2291
Werner N., McNamara B. R., Churazov E., Scannapieco E., 2019, Space Sci. Rev., 215, 5
Young L. M., Bendo G. J., Lucero D. M., 2009, AJ, 137, 3053
Young L. M. et al., 2011, MNRAS, 414, 940
Young L. M. et al., 2014, MNRAS, 444, 3408
Yun M. S., Reddy N. A., Condon J. J., 2001, ApJ, 554, 803

## APPENDIX A: SUPPLEMENTARY MATERIAL

**Table A1.** List of observations for each galaxy and exposure times. In the second column, observation ID is given, for which the total observation time $t_{tot}$ in MOS1, MOS2 and pn detectors is shown in columns 3, 4, and 5, respectively. The useful exposure time $t_{net}$ that is not contaminated by soft-proton flaring is given in the next three columns. The sum of the flaring-excluded exposure times in all instruments together is given in the last column.

| Object | OBSID | $t_{tot}$ (ks) | | | $t_{net}$ (ks) | | | $\sum t_{net}$ (ks) |
|---|---|---|---|---|---|---|---|---|
| | | M1 | M2 | pn | M1 | M2 | pn | |
| NGC 1961 | 0673170101 | 31.5 | 31.5 | 30.4 | 21.5 | 23.5 | 11.3 | – |
| | 0673170301 | 35.0 | 35.1 | 34.0 | 21.2 | 21.1 | 17.5 | – |
| | 0723180101 | 21.8 | 21.8 | 20.8 | 19.8 | 19.6 | 15.9 | – |
| | 0723180201 | 21.6 | 21.5 | 19.9 | 11.9 | 10.6 | 3.0 | – |
| | 0723180301 | 23.9 | 23.8 | 22.7 | 16.3 | 18.1 | 9.3 | – |
| | 0723180401 | 18.6 | 18.8 | 20.7 | 7.1 | 6.6 | 3.3 | – |
| | 0723180601 | 25.6 | 25.5 | 23.9 | 9.1 | 9.8 | 7.0 | – |
| | 0723180701 | 20.9 | 20.8 | 19.2 | 7.3 | 7.5 | 5.5 | – |
| | 0723180801 | 14.7 | 14.6 | 19.0 | 13.6 | 13.6 | 9.7 | – |
| | 0723180901 | 23.2 | 23.1 | 21.5 | 13.2 | 13.7 | 8.9 | 376.7 |
| NGC 3607 | 0099030101 | 22.3 | 22.3 | 20.0 | 15.6 | 17.6 | 10.8 | – |
| | 0693300101 | 44.4 | 44.4 | 43.8 | 31.3 | 35.3 | 19.8 | 130.4 |
| NGC 3665 | 0052140201 | 40.6 | 40.6 | 36.3 | 27.8 | 29.6 | 20.3 | 77.6 |
| NGC 4382 | 0201670101 | 33.5 | 33.5 | 33.2 | 18.8 | 18.8 | 14.4 | – |
| | 0651910401 | 41.7 | 41.6 | 40.6 | 33.6 | 34.1 | 25.7 | – |
| | 0651910501 | 41.2 | 41.3 | 40.2 | 29.9 | 29.6 | 24.1 | – |
| | 0651910601 | 41.2 | 41.1 | 40.1 | 27.7 | 28.7 | 22.1 | – |
| | 0651910701 | 36.5 | 36.5 | 34.9 | 28.3 | 28.3 | 24.2 | 388.3 |
| NGC 4459 | 0550540101 | 81.8 | 81.8 | 82.8 | 72.7 | 73.2 | 60.6 | – |
| | 0550540201 | 20.4 | 20.4 | 18.8 | 18.8 | 18.8 | 15.1 | 259.1 |
| NGC 4526 | 0205010201 | 25.9 | 25.9 | 26.0 | 22.0 | 21.9 | 17.7 | 61.6 |
| NGC 5353 | 0041180401 | 22.3 | 22.3 | 20.0 | 21.3 | 21.1 | 16.8 | 59.1 |

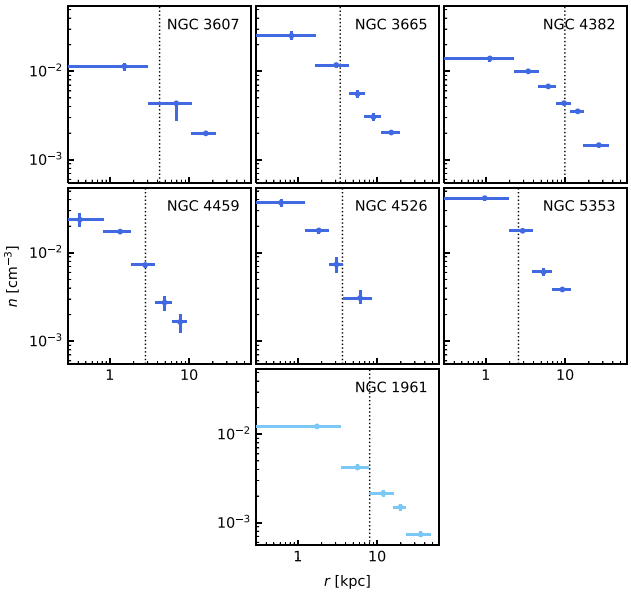


**Figure A1.** Particle density profiles derived from deprojected spectra.

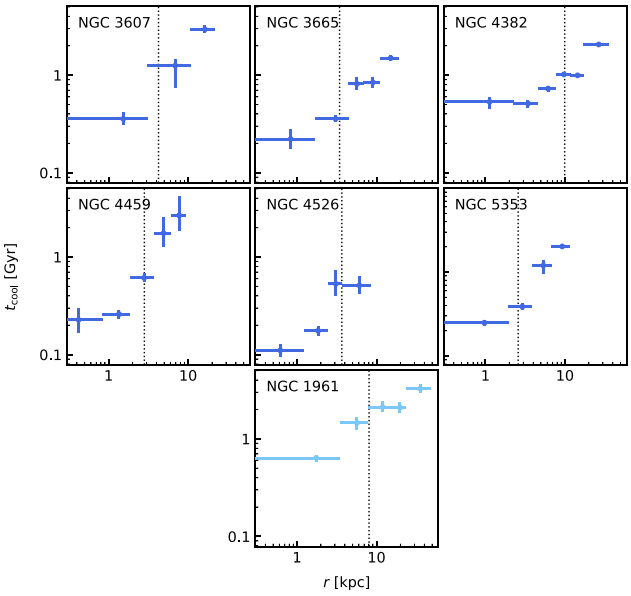


**Figure A2.** Cooling time profiles derived from deprojected spectra.

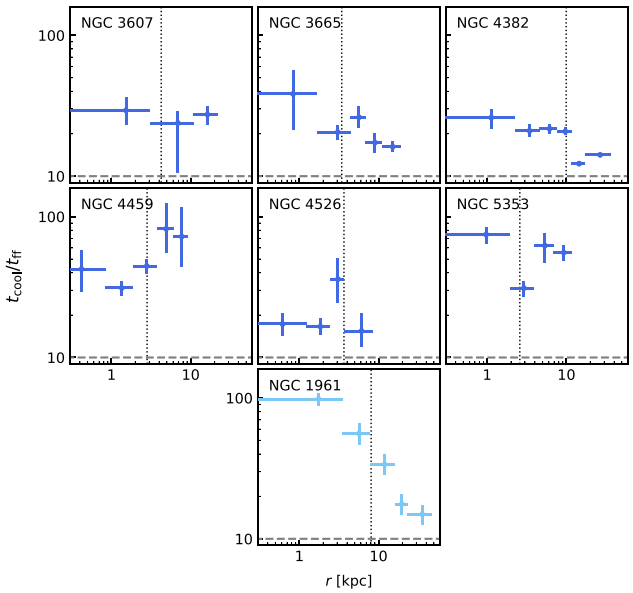


**Figure A3.** Ratio of cooling time to free-fall time. The value $t_{cool}/t_{ff} = 10$ is visualized as a dashed grey line.

This paper has been typeset from a TEX/LATEX file prepared by the author.